

Subpicosecond Optical Stress Generation in Multiferroic BiFeO₃

Hyeon Jun Lee, Youngjun Ahn, Samuel D. Marks, Deepankar Sri Gyan, Eric C. Landahl, Jun Young Lee, Tae Yeon Kim, Sanjith Unithrattil, Sae Hwan Chun, Sunam Kim, Sang-Youn Park, Intae Eom, Carolina Adamo, Darrell G. Schlom, Haidan Wen, Sooheyong Lee, Ji Young Jo, and Paul G. Evans*



Cite This: *Nano Lett.* 2022, 22, 4294–4300



Read Online

ACCESS |



Metrics & More



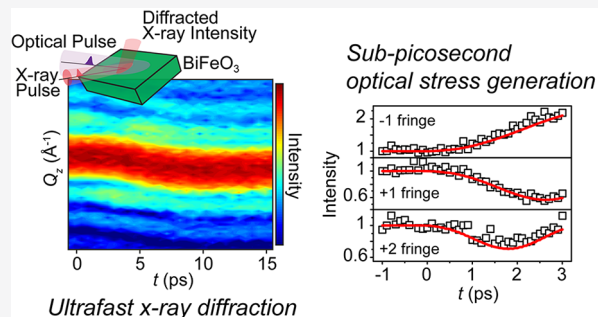
Article Recommendations



Supporting Information

ABSTRACT: Optical excitation leads to ultrafast stress generation in the prototypical multiferroic BiFeO₃. The time scales of stress generation are set by the dynamics of the population of excited electronic states and the coupling of the electronic configuration to the structure. X-ray free-electron laser diffraction reveals high-wavevector subpicosecond-time scale stress generation following ultraviolet excitation of a BiFeO₃ thin film. Stress generation includes a fast component with a 1/e rise time with an upper limit of 300 fs and longer-rise time components extending to 1.5 ps. The contributions of the fast and delayed components vary as a function of optical fluence, with a reduced a fast-component contribution at high fluence. The results provide insight into stress-generation mechanisms linked to the population of excited electrons and point to new directions in the application of nanoscale multiferroics and related ferroic complex oxides. The fast component of the stress indicates that structural parameters and properties of ferroelectric thin film materials can be optically modulated with 3 dB bandwidths of at least 0.5 THz.

KEYWORDS: ultrafast stress, multiferroics, free electron laser dynamics, photoexcitation, nanoscale electronic materials



Visible and ultraviolet light can produce structural responses in semiconductors and insulators that arise from optically induced changes in the population of electronic states. With above-bandgap radiation, the transient population of excited states begins with transitions to electron and hole states that are widely separated in energy from the band-edges and continues in a cascade of intraband transitions to the band edge.^{1–3} Even when the optical excitation involves only a single photon energy, an optical pulse with a large number of photons can induce transitions between many possible pairs of ground and excited states and multiple excited states.¹ The redistribution of the population from the initially populated states occurs on time scales ranging from picoseconds, corresponding to electron–electron or electron–phonon scattering, to much longer time scales associated with electronic traps.^{4,5} The nonequilibrium electron population produces elastic stress with a magnitude depending on the precise nature of populated states and the dynamics of their population, which can vary dramatically in thin-film heterostructures in which the populated states are precisely selected.⁶ The stress contributions are often summarized by local phenomena including the deformation potential or photostriction. The stress depends in detail on the electron population and on the coupling between the electron configuration and the structure. Longer-distance effects are associated with charge separation and depolarization field screening and carrier transport to domain boundaries.^{4,7,8} The

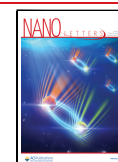
induced stress can lead to a structural distortion that develops over a time scale set by elastic waves propagating with longitudinal acoustic sound velocity.⁹ In ferroelectrics such as BiFeO₃, PbTiO₃, BaTiO₃, and ferroelectric/dielectric superlattices, electronic excitation then produces an overall lattice expansion.^{4,10–12}

The redistribution of electrons among excited electronic states is determined by the electron–phonon coupling time, often on the scale of 1 ps in ferroelectrics.^{4,13} Excited states in oxide ferroelectrics, however, can be expected to have a range of characteristic scattering times, similar to the spectrum of scattering times observed in semiconductors.^{2,3} Furthermore, the coupling of each excited state to the induced changes in the polarization and stress can be different, varying in both sign and magnitude.^{1,14} While the detailed relationship between the electronic configuration and the stress is the subject of continuing theoretical study, the discovery of fast and slower time scale components provides insight into the mechanisms of optically induced stress generation.

Received: December 14, 2021

Revised: May 5, 2022

Published: May 25, 2022



The mismatch between the picosecond and subpicosecond time scales of many of the electronic processes and the longer times associated with overall structural changes poses a challenge to experiments. The optically induced overall expansion of thin films or nanomaterials is coherent over relatively long distances of tens of nanometers and occurs over a time set by the ratio of the size of the system and the longitudinal sound velocity. Typical times for overall expansion are on the order of 10 ps in thin films with thicknesses of tens of nanometers.⁹ Optical-probe experiments often measure the propagation and revival of acoustic pulses and in those cases have structural sensitivity limited to this time scale.¹⁵ Acoustic pulse generation, however, can include a range of frequencies up to the full time-domain bandwidth of the optical pulse.¹⁶ In comparison with optical techniques, ultrafast X-ray scattering measures higher spatial frequencies and thus shorter-range structural distortions. X-ray intensity scattered to wavevectors near Bragg reflections provides insight into shorter-distance correlations and probes faster components of the dynamics.¹⁷ Higher-wavevector contributions to the scattered intensity arise from higher acoustic phonon wavevectors and thus provide insight into faster stress generation mechanisms. Here, ultrafast FEL X-ray diffraction probes the initial stages of the strain generated by a femtosecond-duration above-bandgap optical pulse in the multiferroic complex oxide BiFeO₃. Detailed analysis reveals that there are multiple stress generation time scales following optical excitation. The fast components of the stress generation have characteristic 1/e times less than 300 fs, while longer-time scale contributions extend to more than 1 ps.

Time-resolved diffraction experiments were conducted at the Pohang Accelerator Laboratory X-ray free-electron laser (PAL-XFEL) using the arrangement in Figure 1a.^{18,19} X-ray pulses with 25 fs duration, 9.7 keV photon energy, and 30 Hz repetition rate were focused to a 10 μm full width-at-half-maximum diameter spot. The X-ray fluence was below the damage threshold fluence, which was previously measured to be 1.3×10^6 X-ray photons μm⁻² in these BiFeO₃ layers.²⁰ The measurements spanned a range of wavevectors of 0.1 Å⁻¹ along the Q_z axis of reciprocal space near the BiFeO₃ 002 Bragg reflection, which appears at wavevector $Q_z(002)$ in the pseudocubic notation. The intensity was recorded using the average of 10 FEL X-ray pulses for each measurement setting, normalized by the intensity of each incident pulse. Delay time zero ($t = 0$) was determined with uncertainty less than 100 fs. In comparison with previous studies, this structural method simultaneously determines the speed of sound and accesses the time scales at which stress generation mechanisms can be distinguished. Crucially, diffraction along the crystal truncation rod at $k = Q_z - Q_z(002)$ probes longitudinal acoustic oscillations at a phonon frequency corresponding to wavevector k .¹⁷ The experimental time resolution was much shorter than the acoustic time scales determined by the period of acoustic phonon modes in the range of ΔQ_z considered here.²¹

The 35 nm-thick epitaxial (001)-oriented BiFeO₃ layer was grown by reactive molecular-beam epitaxy on SrTiO₃.²² The BiFeO₃ film was excited using a 50 fs-duration optical pump with a wavelength of 400 nm and a fluence of one to several mJ cm⁻², similar to previous time-resolved diffraction studies.⁴ The pump photon energy, 3.1 eV, is larger than the 2.7 eV optical band gap of BiFeO₃.²² The BiFeO₃ 002 Bragg reflection appears at $Q_z(002) = 3.09 \text{ \AA}^{-1}$ before optical excitation, as inset in Figure 1b, corresponding to an out-of-plane lattice

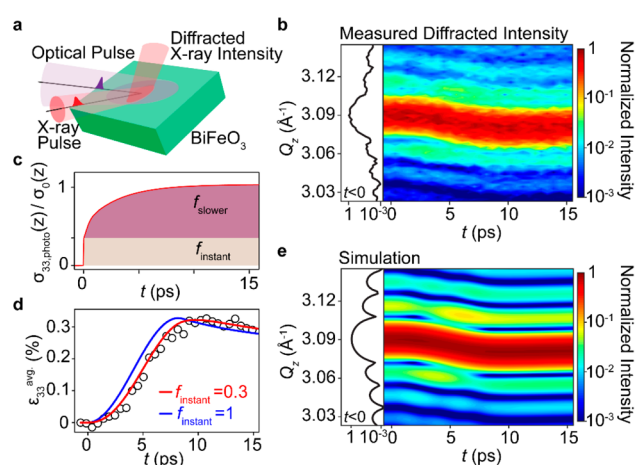


Figure 1. (a) Free-electron-laser X-ray diffraction experiment. (b) Time dependence of the X-ray intensity as a function of Q_z near the BiFeO₃ 002 Bragg reflection following optical excitation at $t = 0$. The diffracted X-ray intensity is normalized to the peak intensity of the 002 reflection at $t < 0$. (c) Model of time dependence of the optically induced out-of-plane stress consisting of instantaneous (f_{instant}) and slower (f_{slower}) stress components. (d) $\epsilon_{33}^{\text{avg}}(t)$ for an optical fluence yielding $\epsilon_{33}^{\text{max}} = 0.32\%$ (points), measured using the shift of the wavevector of maximum intensity in part (b), and simulated $\epsilon_{33}^{\text{avg}}(t)$ for no slower component ($f_{\text{instant}} = 1$) and $f_{\text{instant}} = 0.3$ (lines). (e) Simulated diffracted intensity using stress $\sigma_{33,\text{photo}}(z,t)$ with $f_{\text{instant}} = 0.3$, $f_{\text{slower}} = 0.7$, and $\tau_{\text{slower}} = 1.5$ ps. The measured and simulated diffraction patterns for $t < 0$ are shown in the left panels of (b) and (e).

parameter of 4.067 Å. The thickness fringes have a spacing of 0.018 Å⁻¹, matching the BiFeO₃ film thickness of 35 nm.

The structural distortion resulting from the photoinduced stress is apparent in the X-ray intensity distribution near the BiFeO₃ 002 Bragg reflection in Figure 1b. The wavevector $Q_z(002)$ gradually decreases and reaches a minimum at $t = 9$ ps. The magnitude and time scale of the expansion in Figure 1b are consistent with measurements using a laser-plasma X-ray source and with synchrotron X-ray diffraction studies.^{4,9,23}

Beyond these previous observations, however, a distinctive intensity oscillation at wavevectors away from the diffraction maximum is also apparent in Figure 1b. The elastic response to the photoinduced stress produces an acoustic pulse that propagates through the BiFeO₃ layer and into the substrate at the longitudinal acoustic (LA) sound velocity $v_{LA,[001]pc}$. The notation pc emphasizes that $v_{LA,[001]pc}$ considers the pseudocubic [001] propagation direction, in contrast to the rhombohedral notation considered in studies of acoustic propagation in BiFeO₃ single crystals.^{24,25} The acoustic strain pulse induced by photoinduced stress results in temporal oscillations in the scattered X-ray intensity that are apparent across the entire range of wavevectors in Figure 1b. The disappearance of the temporal oscillations of the scattered intensity after 9 ps indicates that the reflection of the acoustic wave from the interface between the BiFeO₃ film and substrate is negligible (see the Supporting Information).

The generation and propagation of the acoustic pulse were simulated by extending methods previously developed for photoacoustic experiments, as in the Supporting Information.¹⁶ Briefly, the stress employed in the photoacoustic model, i.e., as due to the depth dependence of the optical absorption energy

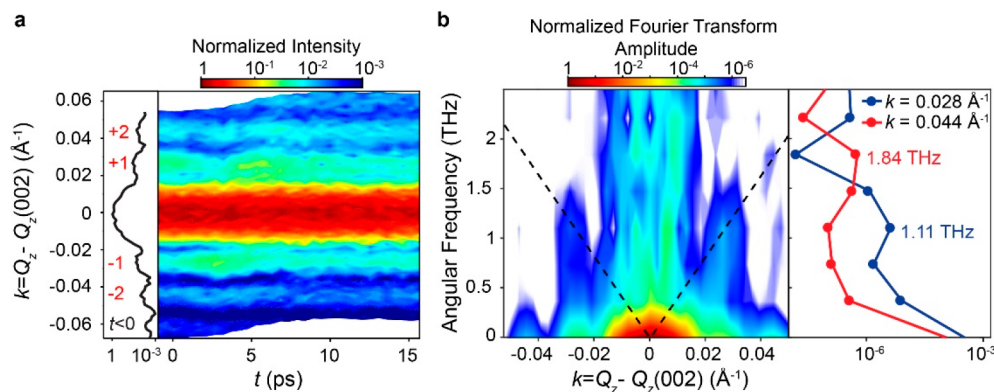


Figure 2. (a) Distribution of scattered X-ray intensity as a function of $k = Q_z - Q_z(002)$. The left panel shows the diffraction pattern of the BiFeO₃ 002 reflection before optical excitation. The thickness fringes are labeled with integer orders ± 1 and ± 2 . (b) Time-domain Fourier transform of the diffracted X-ray intensity shown in (a). The amplitude of the Fourier transform is normalized to 1 at $\omega = 0$ and $k = 0$. The dashed line corresponds to $v_{LA,[001]pc} = 4.1 \text{ km s}^{-1}$. The normalized Fourier transform amplitudes at $k = 0.028$ and 0.044 \AA^{-1} are shown in the right panel.

density, was replaced by a time- and depth-dependent stress profile $\sigma_{33,\text{photo}}(z,t)$.

In order to investigate the key question of the minimum time required for stress generation, we consider a model with only two characteristic times for the generation of the stress. We express the photoinduced out-of-plane stress $\sigma_{33,\text{photo}}(z,t)$ as the sum of an instantaneous stress generated at $t = 0$ and a more slowly generated stress with a $1/e$ rise time τ_{slower} as illustrated in Figure 1c. The stress at time t and depth z in this model is

$$\sigma_{33,\text{photo}}(z, t) = \sigma_0(z)(f_{\text{instant}} + f_{\text{slower}}(1 - e^{-t/\tau_{\text{slower}}})) \quad (1)$$

Here, a fraction f_{instant} of the stress is developed instantaneously, and a complementary fraction f_{slower} occurs with a slow rise time τ_{slower} with $f_{\text{instant}} + f_{\text{slower}} = 1$. The depth profile of the stress, $\sigma_0(z)$, follows the absorption profile of the optical pump, which is proportional to $e^{-z/\zeta}$, where ζ is the optical absorption length in rhombohedral BiFeO₃. The absorption length has not been measured precisely, and we thus adopt the normal incidence value, $\zeta = 35 \text{ nm}$.

The average out-of-plane strain, $\epsilon_{33}^{\text{avg}}(t)$, is defined to be the fractional shift of the wavevector of maximum intensity of the 002 Bragg reflection. Figure 1d shows $\epsilon_{33}^{\text{avg}}(t)$ for an optical fluence giving $\epsilon_{33}^{\text{max}} = 0.33\%$. A time series of diffraction patterns was simulated using kinematic diffraction based on the strain pulse generated by $\sigma_{33,\text{photo}}(z,t)$. A simulation of $\epsilon_{33}^{\text{avg}}(t)$ with $f_{\text{instant}} = 0.3$, $f_{\text{slower}} = 0.7$, and $\tau_{\text{slower}} = 1.5 \text{ ps}$ agrees with the experimentally observed time dependence of $\epsilon_{33}^{\text{avg}}(t)$ in Figure 1d. Simulations with these parameters, in Figure 1e, also reproduce the intensity oscillations across the range of X-ray wavevectors.

The time evolution of the average strain in Figure 1d indicates that contributions to the stress have characteristic rise times ranging from effectively instantaneous on the time scale of these measurements to on the order of picoseconds. The existence of multiple characteristic times is illustrated by the simulation with $f_{\text{instant}} = 1$ and $f_{\text{slower}} = 0$, also in Figure 1d, corresponding to a completely instantaneously developed photoinduced stress. The simulated strain with $f_{\text{instant}} = 1$ develops faster evolution than the measurements and is a poor fit for the results.

The value of $v_{LA,[001]pc}$ is crucial in comparing the measurement and the simulation. The temporal oscillations

in the measured intensity in Figure 1b have a frequency that increases as a function of the wavevector difference from $Q_z(002)$. Each thickness fringe oscillates with a temporal frequency set by the corresponding phonon mode and with a phase that is set by the depth dependence of the strain profile. Figure 2a shows the intensity distribution plotted in terms of $k = Q_z - Q_z(002)$, emphasizing this effect. The acoustic phonon dispersion can be visualized using the time-domain Fourier transform of the diffracted intensity, as in Figure 2b. The temporal oscillations of the intensity at $k = \pm 0.028$ and 0.044 \AA^{-1} , corresponding to the thickness fringes with indices ± 1 and ± 2 , have angular frequencies ω of 1.11 THz and 1.84 THz, respectively. The dispersion exhibits a wavevector-frequency relationship fit well by a line with slope $v_{LA,[001]pc} = 4.1 \text{ km s}^{-1}$. The value of $v_{LA,[001]pc}$ from Figure 2b is at the low end of the range reported for BiFeO₃ single crystals and polycrystalline specimens.^{25–27} This measurement of the velocity allows the time scales of the stress generation to be determined precisely. Further discussion of $v_{LA,[001]pc}$, the effect of the multidomain sample configuration, and previous measurements are in the Supporting Information.

A transverse acoustic (TA) pulse generated by optically induced shear strain, in principle, could contribute to the slow evolution of average strain. The TA sound velocity is slower than $v_{LA,[001]pc}$ and has been previously observed to account for up to 0.15 of the optically induced strain in single crystals.²⁸ The average strain obtained in a simulation in which the TA strain is used instead of the slower component evolves faster than the measurements and is a poor fit for the results. We thus conclude that an instantaneously generated TA strain pulse does not account for the slowly generated strain component. It remains possible, however, that the mechanism responsible for the delayed generation of strain produces both longitudinal and transverse pulses, as observed in the single-crystal samples.²⁸

The difference in the optical excitation due to birefringence could lead to different amplitudes of the stress in each of the domain variants and perhaps to the propagation of acoustic pulses among them. The acoustic pulse propagation between domains would occur in a time determined from the acoustic velocity and the characteristic domain size of 100 nm.²⁹ For the longitudinal acoustic mode, the propagation time is on the order of 25 ps, greater than the total time range of our study. We thus expect that the effect of strain propagation through

four variants on the ultrafast characteristic time will not contribute to the effects reported here.

The uncertainty in f_{instant} , f_{slower} , and τ_{slower} was determined by comparing the experiment and simulation. The temporal oscillations of the intensity at the wavevectors of the thickness fringes with indices -1 , $+1$, and $+2$ are shown in Figure 3a for

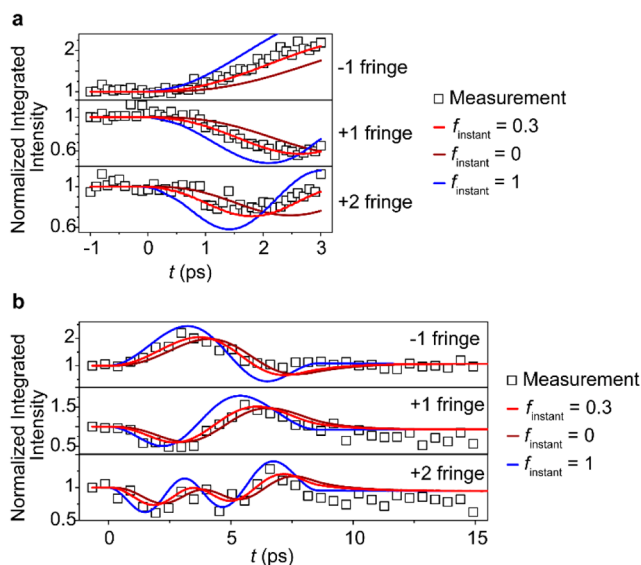


Figure 3. Measured normalized integrated intensities of -1 , $+1$, and $+2$ thickness fringes (points) and simulations with $f_{\text{instant}} = 0, 0.3$, and 1 (lines) in time ranges (a) up to 3 ps with $\epsilon_{33}^{\text{max}} = 0.35\%$ and (b) up to 15 ps with $\epsilon_{33}^{\text{max}} = 0.32\%$.

the time range up to 3 ps for an optical fluence yielding $\epsilon_{33}^{\text{max}} = 0.35\%$. Figure 3a also shows the intensity predicted by a simulation with $f_{\text{instant}} = 0.3$ and $\tau_{\text{slower}} = 1.5$ ps, which accurately reproduces the time dependence. Figure 3b shows that the same parameters fit throughout the entire range of times of the acoustic response, up to 15 ps. Figure 3 also includes simulations using other values of f_{instant} that provide a poor fit to the intensity variation. The intensities are fit poorly with for both $f_{\text{instant}} = 0$ and $f_{\text{instant}} = 1$, indicating that there is a spectrum of time scales for the generation of the stress. The root-mean-square difference between simulation and experiment reaches a minimum for $f_{\text{instant}} = 0.3$ and provides equally good agreement for values of $f_{\text{instant}} = 0.25$ to 0.4 .

The intensities of the thickness fringes allow an upper limit to be placed on the characteristic rise time τ_{instant} of the instantaneous component. Note that the average strain $\epsilon_{33}^{\text{avg}}(t)$ is comparatively insensitive to the subpicosecond rise time of the instantaneous stress because of the long 9 ps time scale for overall expansion. Figure 4a shows the measured $\epsilon_{33}^{\text{avg}}(t)$ and simulations with $\tau_{\text{instant}} = 0$ and 300 fs. The difference between simulations of $\epsilon_{33}^{\text{avg}}(t)$ for different values of the rise time of the instantaneous stress is small, as expected from the low-frequency dynamics probed by the average strain. The intensities of the thickness fringes are more far sensitive to the rise time of the instantaneous component of the stress. The measured and simulated intensities of the -1 , $+1$, and $+2$ thickness fringes are shown in Figure 4b for up to 3 ps. The measurements show a qualitatively better fit for zero rise time than for 300 fs, indicating that the stress generation extends to times below 300 fs.

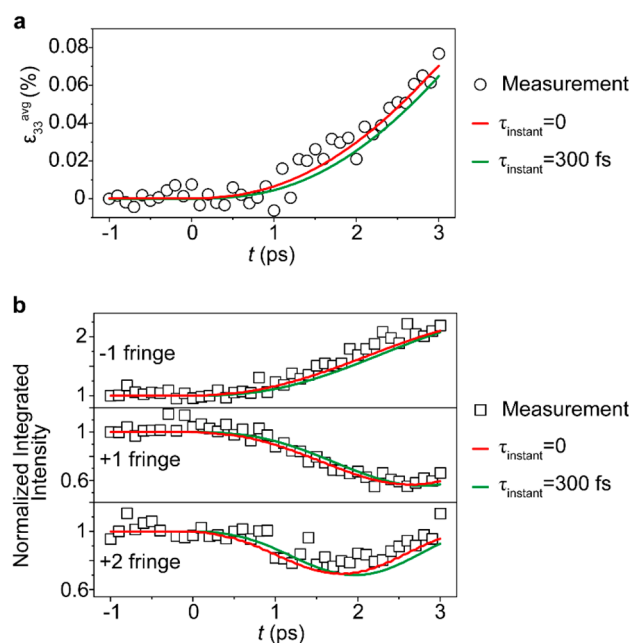


Figure 4. Measurements (points) of (a) $\epsilon_{33}^{\text{avg}}(t)$ and (b) intensities of -1 , $+1$, and $+2$ thickness fringes for the time range -1 to 3 ps with $\epsilon_{33}^{\text{max}} = 0.35\%$. Solid lines show the simulated intensities resulting from instantaneous strain generation rise times of 0 and 300 fs.

The fractional contributions of the slower and instantaneous components depend on the optical fluence, providing insight into the mechanisms of the stress generation. $\epsilon_{33}^{\text{max}}$ was varied from 0.11% to 0.84% by repeating the experiments for different incident optical fluences, resulting in the measurements of $\epsilon_{33}^{\text{avg}}(t)$ in Figure 5a. The observations are matched by

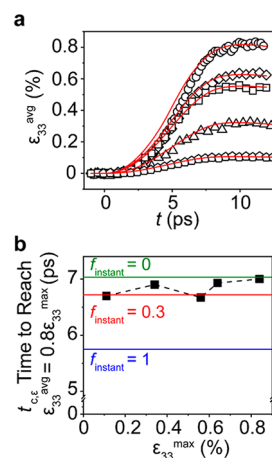


Figure 5. (a) Measured (points) and simulated (lines) values of $\epsilon_{33}^{\text{avg}}(t)$ for $\epsilon_{33}^{\text{max}} = 0.11\%$, 0.32% , 0.56% , and 0.84% . The simulations use $f_{\text{instant}} = 0.3$. (b) Time $t_{c,\epsilon}$ to reach $\epsilon_{33}^{\text{avg}}(t) = 0.8 \epsilon_{33}^{\text{max}}$ as a function of $\epsilon_{33}^{\text{max}}$. The lines indicate values of $t_{c,\epsilon}$ obtained in simulations with $f_{\text{instant}} = 0, 0.3$, and 1 .

simulations with $f_{\text{instant}} = 0.3$ for values of $\epsilon_{33}^{\text{max}}$ up to 0.6% , also shown in Figure 5a. At $\epsilon_{33}^{\text{max}}$ above 0.6% , the simulation with $f_{\text{instant}} = 0.3$ has a systematically more rapid increase in $\epsilon_{33}^{\text{avg}}(t)$ than the observation. There is thus a reduction in the instantaneous contribution to the stress at the highest fluences. To quantify the fluence dependence, we have measured $t_{c,\epsilon}$,

defined to be the characteristic time to reach 80% of ϵ_{33}^{\max} . Figure 5b shows measured values of $t_{c,e}$ and the results of simulations with $f_{\text{instant}} = 0, 0.3, \text{ and } 1$. The simulated values of $t_{c,e}$ match predictions for $f_{\text{instant}} = 0.3$ for low incident optical fluences but require smaller f_{instant} at large amplitudes of the maximum strain. The instantaneous component thus apparently saturates at $\epsilon_{33}^{\max} = 0.6\%$ or an instantaneous stress induced strain of 0.2%.

We associate the fast component of the stress with the rapid redistribution of the electron population after the absorption of the optical pulse. The experiments reported here allow more general predictions of the stress arising from the population of specific states to be evaluated. Density functional theory calculations have considered the case in which the photon energy connects particular examples of occupied and unoccupied states.¹ The stress resulting from excitation at the different photon energies varies in both sign and direction.¹ The photon energy of the present experiments is higher than considered in ref 1, which allows transitions between a wider range of pairs of occupied and unoccupied states. A detailed comparison between the experiments here and the photostriction mechanism probed in ref 1 is difficult because the states populated in the present study differ and vary rapidly after excitation.

Similarly, predictions of the shift current effect in BiFeO₃ reveal that the polarization (and resulting in stress) arising from the coherent state produced during the optical pulse depend on the direction, photon energy, and polarization of the optical field.¹⁴ Again, the range of states connected by transitions between states with an energy difference matching the photon energy of the excitation complicates the predictions. The shift current effect further depends on the direction of the optical wavevector with respect to the crystallographic axes and thus can be different for the four domain variants present in the BiFeO₃ layer studied here. Despite the difficulty in establishing the comparison with the photostriction and shift current mechanisms, however, it is clear that a rapid stress generation mechanism is apparent in the experimental data.

The slower component of the stress involves the drift of the carriers in the built-in electric field and multiple scattering events including electron–electron and electron–phonon scattering. The relative magnitudes of the slower time scale effects have been previously studied and linked to heating and field screening.^{4,5} For example, at longer time scales, the sign of the stress developed in GaAs and PbTiO₃ can depend on the direction of the built-in polarization.^{7,30}

The reduction in the relative magnitude of the fast component at high fluence may arise from a change in the distribution of electrons among the excited states at high pump fluence due to increased electron–electron scattering or depletion of the ground state population distribution. The area concentration of excited charge carriers at the highest optical fluence is $w_{\text{opt}}/E_{\text{opt}}$ where w_{opt} is the absorbed fluence and E_{opt} is the optical photon energy. For $w_{\text{opt}} = 3 \text{ mJ cm}^{-2}$ and $E_{\text{opt}} = 3.1 \text{ eV}$, the excited carrier density is $6 \times 10^{15} \text{ cm}^{-2}$. The calculated total density of states of BiFeO₃ near the valence band edge is 8.4 eV^{-1} per formula unit.^{31,32} This can be regarded as an upper limit of the density of states available to serve as the ground state for absorption because the optical transition may involve a subset of the states. The energy difference between the bandgap and the photon energy is 0.4 eV. States within this energy difference from the band edge can

serve as the ground state for absorption. The BiFeO₃ layer thus has $(1.4 \times 10^{23} \text{ eV}^{-1} \text{ cm}^{-3})(0.4 \text{ eV})(35 \text{ nm}) = 2 \times 10^{17} \text{ cm}^{-2}$ electrons in the energy range available for absorption. The carrier densities excited at the optical excitation fluences reach on the order of several percent of the available electrons and may thus lead to a perturbation of the optical properties. Even in the case where the overall absorption is not reduced by the excitation of a large concentration of electrons, a difference in the spectrum of states populated after optical excitation between the lowest and highest fluences could result in a difference in the resulting stress and increase the apparent component of the slower rise time contribution.

In conclusion, the stress generated at ultrafast time scales in BiFeO₃ is more precisely probed in high-dynamic-range X-ray diffraction experiments than has been possible in previous X-ray or ultrafast optical studies. The results provide insight into the mechanisms responsible for generating the stress, including an instantaneous time scale less than 300 fs and a saturation of the instantaneous component at high optical fluences. An exciting future possibility is that mode-selective optical excitation populating specific excited states or combinations of excited states can be used to test specific mechanisms. Similarly, the use of 111-oriented or single domain BiFeO₃ may allow the origins of the fast transient to be separated by reducing the structural complexity of the sample. For technological applications in transducers and actuators, the upper limit of 300 fs for the stress generation established in the present measurements indicates that 3 dB bandwidths on the order of at least 0.5 THz will be available for stress generation in BiFeO₃ and other oxide materials. The generation of stress at this time scale has potential implications for optical control of materials properties via controlled structural deformation, including the modulation of magnetic, electronic, and optical properties linked to the structure. Building on these results, the polarization of 2D materials may provide a mechanism to induce high-bandwidth stress generation.³³

■ ASSOCIATED CONTENT

SI Supporting Information

The Supporting Information is available free of charge at <https://pubs.acs.org/doi/10.1021/acs.nanolett.1c04831>.

Simulations of stress generation, acoustic pulse propagation, and X-ray scattering; analysis of model fitting; comparison of measured sound velocity with literature values (PDF)

■ AUTHOR INFORMATION

Corresponding Author

Paul G. Evans – Department of Materials Science and Engineering, University of Wisconsin–Madison, Madison, Wisconsin 53706, United States; orcid.org/0000-0003-0421-6792; Email: pgevans@wisc.edu

Authors

Hyeon Jun Lee – Department of Materials Science and Engineering, University of Wisconsin–Madison, Madison, Wisconsin 53706, United States; orcid.org/0000-0001-8202-6471

Youngjun Ahn – Department of Materials Science and Engineering, University of Wisconsin–Madison, Madison, Wisconsin 53706, United States

- Samuel D. Marks** – Department of Materials Science and Engineering, University of Wisconsin–Madison, Madison, Wisconsin 53706, United States; orcid.org/0000-0001-6677-3274
- Deepankar Sri Gyan** – Department of Materials Science and Engineering, University of Wisconsin–Madison, Madison, Wisconsin 53706, United States
- Eric C. Landahl** – Department of Physics, DePaul University, Chicago, Illinois 60614, United States
- Jun Young Lee** – School of Materials Science and Engineering, Gwangju Institute of Science and Technology, Gwangju 61005, South Korea
- Tae Yeon Kim** – School of Materials Science and Engineering, Gwangju Institute of Science and Technology, Gwangju 61005, South Korea
- Sanjith Unithrattil** – School of Materials Science and Engineering, Gwangju Institute of Science and Technology, Gwangju 61005, South Korea; orcid.org/0000-0001-9072-7163
- Sae Hwan Chun** – Pohang Accelerator Laboratory, Pohang, Gyeongbuk 37673, South Korea
- Sunam Kim** – Pohang Accelerator Laboratory, Pohang, Gyeongbuk 37673, South Korea
- Sang-Youn Park** – Pohang Accelerator Laboratory, Pohang, Gyeongbuk 37673, South Korea
- Intae Eom** – Pohang Accelerator Laboratory, Pohang, Gyeongbuk 37673, South Korea
- Carolina Adamo** – Department of Materials Science and Engineering, Cornell University, Ithaca, New York 14853, United States; Present Address: Northrop Grumman Corporation, 1 Space Park, Redondo Beach, CA 90278
- Darrell G. Schlom** – Department of Materials Science and Engineering, Cornell University, Ithaca, New York 14853, United States; Kavli Institute at Cornell for Nanoscale Science, Ithaca, New York 14853, United States; Leibniz-Institut für Kristallzüchtung, 12489 Berlin, Germany; orcid.org/0000-0003-2493-6113
- Haidan Wen** – Materials Science Division and X-ray Science Division, Argonne National Laboratory, Argonne, Illinois 60439, United States; orcid.org/0000-0002-5427-175X
- Sooheyong Lee** – Korea Research Institute of Standards and Science, Daejeon 34113, South Korea; Department of Nano Science, University of Science and Technology, Daejeon 34113, South Korea
- Ji Young Jo** – School of Materials Science and Engineering, Gwangju Institute of Science and Technology, Gwangju 61005, South Korea; orcid.org/0000-0001-9873-3525

Complete contact information is available at:

<https://pubs.acs.org/10.1021/acs.nanolett.1c04831>

Author Contributions

H.J.L. and P.G.E. designed the experiments. H.J.L., Y.A., S.D.M., E.C.L., J.Y.L., T.Y.K., S.U., S.H.C., S.K., S.-Y.P., I. E., S.L., J.Y.J., and P.G.E. carried out the time-resolved free-electron-laser X-ray diffraction experiments. H.J.L. analyzed the scattering data and developed the supporting calculations. C.A. synthesized the sample with advice from D.G.S. H.W. and D.S.G. contributed to the discussion and development of the stress generation model. The manuscript was written with contributions from all authors. All authors have given approval to the final version of the manuscript.

Notes

The authors declare no competing financial interest.

ACKNOWLEDGMENTS

The authors gratefully acknowledge support from the U.S. DOE, Basic Energy Sciences, Materials Sciences and Engineering, under contract no. DE-FG02-04ER46147. S.D.M. acknowledges support from the University of Wisconsin Materials Research Science and Engineering Center (DMR-1720415). H.W. acknowledges support by the U.S. Department of Energy, Office of Basic Energy Sciences, Materials Science and Engineering Division. D.G.S. acknowledges support from the U.S. DOE through contract SC0019414. The experiment was performed at the XSS beamline of PAL-XFEL (proposal no. 2018-1st-XSS-003) funded by the Ministry of Science and ICT of Korea. S.L. was supported by the National Research Foundation of Korea under contract No. NRF-2019K1A3A7A09033397. This research was supported by the National Research Foundation of Korea (NRF) grants funded by the Korean government (MSIP) (NRF-2020R1A2C2006127 and NRF-2021R1A5A1032996) and funded by the Creative Materials Discovery Program of Ministry of Science and ICT (2017M3D1A1040828) and the GIST Research Institute (GRI) grant funded by the GIST.

REFERENCES

- (1) Paillard, C.; Xu, B.; Dkhil, B.; Geneste, G.; Bellaiche, L. Photostriction in Ferroelectrics from Density Functional Theory. *Phys. Rev. Lett.* **2016**, *116* (24), 247401.
- (2) Elsaesser, T.; Shah, J.; Rota, L.; Lugli, P. Initial Thermalization of Photoexcited Carriers in GaAs Studied by Femtosecond Luminescence Spectroscopy. *Phys. Rev. Lett.* **1991**, *66* (13), 1757–1760.
- (3) Snoke, D. W.; Rühle, W. W.; Lu, Y. C.; Bauser, E. Evolution of a Nonthermal Electron Energy Distribution in GaAs. *Phys. Rev. B* **1992**, *45* (19), 10979–10989.
- (4) Wen, H.; Chen, P.; Cosgriff, M. P.; Walko, D. A.; Lee, J. H.; Adamo, C.; Schaller, R. D.; Ihlefeld, J. F.; Dufresne, E. M.; Schlom, D. G.; Evans, P. G.; Freeland, J. W.; Li, Y. Electronic Origin of Ultrafast Photoinduced Strain in BiFeO₃. *Phys. Rev. Lett.* **2013**, *110* (3), 037601.
- (5) Sheu, Y. M.; Trugman, S. A.; Park, Y.-S.; Lee, S.; Yi, H. T.; Cheong, S.-W.; Jia, Q. X.; Taylor, A. J.; Prasankumar, R. P. Ultrafast Carrier Dynamics and Radiative Recombination in Multiferroic BiFeO₃. *Appl. Phys. Lett.* **2012**, *100* (24), 242904.
- (6) Lee, S.; Jo, W.; DiChiara, A. D.; Holmes, T. P.; Santowski, S.; Cho, Y. C.; Landahl, E. C. Probing Electronic Strain Generation by Separated Electron-Hole Pairs Using Time-Resolved X-ray Scattering. *Appl. Sci.* **2019**, *9* (22), 4788.
- (7) Matzen, S.; Guillemot, L.; Maroutian, T.; Patel, S. K. K.; Wen, H. D.; DiChiara, A. D.; Agnus, G.; Shpyrko, O. G.; Fullerton, E. E.; Ravelosona, D.; Lecoeur, P.; Kukreja, R. Tuning Ultrafast Photoinduced Strain in Ferroelectric-Based Devices. *Adv. Electron. Mater.* **2019**, *5* (6), 1800709.
- (8) Guzelurk, B.; Mei, A. B.; Zhang, L.; Tan, L. Z.; Donahue, P.; Singh, A. G.; Schlom, D. G.; Martin, L. W.; Lindenberg, A. M. Light-Induced Currents at Domain Walls in Multiferroic BiFeO₃. *Nano Lett.* **2020**, *20* (1), 145–151.
- (9) Schick, D.; Herzog, M.; Wen, H.; Chen, P.; Adamo, C.; Gaal, P.; Schlom, D. G.; Evans, P. G.; Li, Y.; Bargheer, M. Localized Excited Charge Carriers Generate Ultrafast Inhomogeneous Strain in the Multiferroic BiFeO₃. *Phys. Rev. Lett.* **2014**, *112* (9), 097602.
- (10) Daranciang, D.; Highland, M. J.; Wen, H. D.; Young, S. M.; Brandt, N. C.; Hwang, H. Y.; Vattilana, M.; Nicoul, M.; Quirin, F.; Goodfellow, J.; Qi, T. T.; Grinberg, I.; Fritz, D. M.; Cammarata, M.; Zhu, D. L.; Lemke, H. T.; Walko, D. A.; Dufresne, E. M.; Li, Y. L.; Larsson, J.; Reis, D. A.; Sokolowski-Tinten, K.; Nelson, K. A.; Rappe,

- A. M.; Fuoss, P. H.; Stephenson, G. B.; Lindenberg, A. M. Ultrafast Photovoltaic Response in Ferroelectric Nanolayers. *Phys. Rev. Lett.* **2012**, *108* (8), 087601.
- (11) Ahn, Y.; Everhardt, A. S.; Lee, H. J.; Park, J.; Pateras, A.; Damerio, S.; Zhou, T.; DiChiara, A. D.; Wen, H. D.; Noheda, B.; Evans, P. G. Dynamic Tilting of Ferroelectric Domain Walls Caused by Optically Induced Electronic Screening. *Phys. Rev. Lett.* **2021**, *127* (9), 097402.
- (12) Lee, H. J.; Ahn, Y.; Marks, S. D.; Landahl, E. C.; Zhuang, S. H.; Yusuf, M. H.; Dawber, M.; Lee, J. Y.; Kim, T. Y.; Unithrattil, S.; Chun, S. H.; Kim, S.; Eom, I.; Park, S. Y.; Kim, K. S.; Lee, S.; Jo, J. Y.; Hu, J. M.; Evans, P. G. Structural Evidence for Ultrafast Polarization Rotation in Ferroelectric/Dielectric Superlattice Nanodomains. *Phys. Rev. X* **2021**, *11* (3), 031031.
- (13) Zhang, Z.; Jin, Z.; Pan, Q.; Xu, Y.; Lin, X.; Ma, G.; Cheng, Z. Temperature Dependent Photoexcited Carrier Dynamics in Multiferroic BiFeO₃ Film: A Hidden Phase Transition. *Appl. Phys. Lett.* **2014**, *104* (15), 151902.
- (14) Young, S. M.; Zheng, F.; Rappe, A. M. First-Principles Calculation of the Bulk Photovoltaic Effect in Bismuth Ferrite. *Phys. Rev. Lett.* **2012**, *109* (23), 236601.
- (15) Ruello, P.; Gusev, V. E. Physical Mechanisms of Coherent Acoustic Phonons Generation by Ultrafast Laser Action. *Ultrasonics* **2015**, *56*, 21–35.
- (16) Thomsen, C.; Grahn, H. T.; Maris, H. J.; Tauc, J. Surface Generation and Detection of Phonons by Picosecond Light Pulses. *Phys. Rev. B* **1986**, *34* (6), 4129–4138.
- (17) Reis, D. A.; DeCamp, M. F.; Bucksbaum, P. H.; Clarke, R.; Dufresne, E.; Hertlein, M.; Merlin, R.; Falcone, R.; Kapteyn, H.; Murnane, M. M.; Larsson, J.; Missalla, T.; Wark, J. S. Probing Impulsive Strain Propagation with X-Ray Pulses. *Phys. Rev. Lett.* **2001**, *86* (14), 3072–3075.
- (18) McNeil, B. W. J.; Thompson, N. R. X-ray Free-Electron Lasers. *Nat. Photonics* **2010**, *4*, 814–821.
- (19) Kang, H.-S.; Min, C.-K.; Heo, H.; Kim, C.; Yang, H.; Kim, G.; Nam, I.; Baek, S. Y.; Choi, H.-J.; Mun, G.; Park, B. R.; Suh, Y. J.; Shin, D. C.; Hu, J.; Hong, J.; Jung, S.; Kim, S.-H.; Kim, K.; Na, D.; Park, S. S.; Park, Y. J.; Han, J.-H.; Jung, Y. G.; Jeong, S. H.; Lee, H. G.; Lee, S.; Lee, S.; Lee, W.-W.; Oh, B.; Suh, H. S.; Parc, Y. W.; Park, S.-J.; Kim, M. H.; Jung, N.-S.; Kim, Y.-C.; Lee, M.-S.; Lee, B.-H.; Sung, C.-W.; Mok, I.-S.; Yang, J.-M.; Lee, C.-S.; Shin, H.; Kim, J. H.; Kim, Y.; Lee, J. H.; Park, S.-Y.; Kim, J.; Park, J.; Eom, I.; Rah, S.; Kim, S.; Nam, K. H.; Park, J.; Park, J.; Kim, S.; Kwon, S.; Park, S. H.; Kim, K. S.; Hyun, H.; Kim, S. N.; Kim, S.; Hwang, S.-M.; Kim, M. J.; Lim, C.-Y.; Yu, C.-J.; Kim, B.-S.; Kang, T.-H.; Kim, K.-W.; Kim, S.-H.; Lee, H.-S.; Lee, H.-S.; Park, K.-H.; Koo, T.-Y.; Kim, D.-E.; Ko, I. S. Hard X-ray Free-Electron Laser with Femtosecond-Scale Timing Jitter. *Nat. Photonics* **2017**, *11* (11), 708–713.
- (20) Lee, H. J.; Ahn, Y.; Marks, S. D.; Landahl, E. C.; Lee, J. Y.; Kim, T. Y.; Unithrattil, S.; Jo, J. Y.; Chun, S. H.; Kim, S.; Park, S.-Y.; Eom, I.; Adamo, C.; Schlom, D. G.; Wen, H.; Evans, P. G. Non-Thermal Fluence Threshold for Femtosecond Pulsed X-ray Radiation Damage in Perovskite Complex Oxide Epitaxial Heterostructures. *Appl. Phys. Lett.* **2019**, *115* (25), 252903.
- (21) Schick, D.; Herzog, M.; Bojahr, A.; Leitenberger, W.; Hertwig, A.; Shayduk, R.; Bargheer, M. Ultrafast Lattice Response of Photoexcited Thin Films Studied by X-ray Diffraction. *Struct. Dyn.* **2014**, *1* (6), 064501.
- (22) Ihlefeld, J. F.; Podraza, N. J.; Liu, Z. K.; Rai, R. C.; Xu, X.; Heeg, T.; Chen, Y. B.; Li, J.; Collins, R. W.; Musfeldt, J. L.; Pan, X. Q.; Schubert, J.; Ramesh, R.; Schlom, D. G. Optical Band Gap of BiFeO₃ Grown by Molecular-Beam Epitaxy. *Appl. Phys. Lett.* **2008**, *92* (14), 142908.
- (23) Li, Y. L.; Adamo, C.; Chen, P.; Evans, P. G.; Nakhmanson, S. M.; Parker, W.; Rowland, C. E.; Schaller, R. D.; Schlom, D. G.; Walko, D. A.; Wen, H.; Zhang, Q. Giant Optical Enhancement of Strain Gradient in Ferroelectric BiFeO₃ Thin Films and its Physical Origin. *Sci. Rep.* **2015**, *5*, 16650.
- (24) Ruello, P.; Pezeril, T.; Avanesyan, S.; Vaudel, G.; Gusev, V.; Infante, I. C.; Dkhil, B. Photoexcitation of Gigahertz Longitudinal and Shear Acoustic Waves in BiFeO₃ Multiferroic Single Crystal. *Appl. Phys. Lett.* **2012**, *100* (21), 212906.
- (25) Smirnova, E. P.; Sotnikov, A.; Ktitorov, S.; Zaitseva, N.; Schmidt, H.; Weihnacht, M. Acoustic Properties of Multiferroic BiFeO₃ over the Temperature Range 4.2–830 K. *Euro. Phys. J. B* **2011**, *83* (1), 39.
- (26) Hemme, P.; Djemia, P.; Rovillain, P.; Gallais, Y.; Sacuto, A.; Forget, A.; Colson, D.; Charron, E.; Perrin, B.; Belliard, L.; Cazayous, M. Elastic Properties Assessment in the Multiferroic BiFeO₃ by Pump and Probe Method. *Appl. Phys. Lett.* **2021**, *118* (6), 062902.
- (27) Borissenko, E.; Goffinet, M.; Bosak, A.; Rovillain, P.; Cazayous, M.; Colson, D.; Ghosez, P.; Krisch, M. Lattice Dynamics of Multiferroic BiFeO₃ Studied by Inelastic X-ray Scattering. *J. Phys.: Condens. Matter* **2013**, *25* (10), 102201.
- (28) Juve, V.; Gu, R.; Gable, S.; Maroutian, T.; Vaudel, G.; Matzen, S.; Chigarev, N.; Raetz, S.; Gusev, V. E.; Viret, M.; Jarnac, A.; Laulhe, C.; Maznev, A. A.; Dkhil, B.; Ruello, P. Ultrafast Light-Induced Shear Strain Probed by Time-Resolved X-Ray Diffraction: Multiferroic BiFeO₃ as a Case Study. *Phys. Rev. B* **2020**, *102* (22), 220303.
- (29) Catalan, G.; Béa, H.; Fusil, S.; Bibes, M.; Paruch, P.; Barthélémy, A.; Scott, J. F. Fractal Dimension and Size Scaling of Domains in Thin Films of Multiferroic BiFeO₃. *Phys. Rev. Lett.* **2008**, *100* (2), 027602.
- (30) Babilotte, P.; Ruello, P.; Pezeril, T.; Vaudel, G.; Mounier, D.; Breteau, J. M.; Gusev, V. Transition from Piezoelectric to Deformation Potential Mechanism of Hypersound Photogeneration in n-doped GaAs Semiconductors. *J. Appl. Phys.* **2011**, *109* (6), 064909.
- (31) Ravindran, P.; Vidya, R.; Kjekshus, A.; Fjellvag, H.; Eriksson, O. Theoretical Investigation of Magnetoelectric Behavior in BiFeO₃. *Phys. Rev. B* **2006**, *74* (22), 224412.
- (32) Liu, K.; Fan, H. Q.; Ren, P. R.; Yang, C. Structural, Electronic and Optical Properties of BiFeO₃ Studied by First-Principles. *J. Alloys Compd.* **2011**, *509* (5), 1901–1905.
- (33) Dai, Y.; Zheng, Q.; Ziffer, M. E.; Rhodes, D.; Hone, J.; Zhao, J.; Zhu, X. Ultrafast Ferroelectric Ordering on the Surface of a Topological Semimetal MoTe₂. *Nano Lett.* **2021**, *21* (23), 9903–9908.